Numerical simulations of the flow around two tandem airfoils near a flat surface

Bo Yin[1], Yu Guan[1*], Wen Ao[2*], Peijin Liu[2], Nader Karimi[3], Mohammad Hossein Doranehgard[4]

[1]Department of Mechanical and Aerospace Engineering, The Hong Kong University of Science and Technology, Clear Water Bay, Hong Kong

[2]Science and Technology on Combustion, Internal Flow and Thermo-structure Laboratory, Northwestern Polytechnical University, Xi'an 710072, China

[3]School of Engineering and Materials Science, Queen Mary University of London, London E1 4NS, United Kingdom

[4]Department of Civil and Environmental Engineering, School of Mining and Petroleum Engineering, University of Alberta, Edmonton, Alberta, T6G 1H9, Canada

[*]Corresponding authors: Yu Guan (yguanad@connect.ust.hk), Wen Ao (aw@nwpu.edu.cn)

Abstract

The advent of pico-aerial vehicles (PAVs) for thermal surveillance has necessitated a better understanding of the flow field around airfoils at low Reynolds numbers (typically on the order of 10^2 to 10^3) owing to the small length and velocity scales associated with PAVs. Previous studies have shown that two airfoils arranged in a tandem configuration can exhibit better aerodynamic performance than two identical airfoils in isolation, but this has only been explored at relatively high Reynolds numbers (around 10^5 and above). In this parametric study, we numerically simulate the two-dimensional flow field around two tandem NACA 0012 airfoils in ground effect, at a Reynolds number low enough to be relevant to PAV conditions ($Re = 500$). With the angle of attack fixed at $\alpha = 5^{\circ}$ on both the fore and aft airfoils, we investigate the effects of three control parameters, namely the stagger distance, the gap height, and the ground clearance. Results show that, consistent with previous studies at higher Re, the two tandem airfoils are more aerodynamically efficient than two identical airfoils in isolation, especially when the fore airfoil is higher than the aft airfoil. The aerodynamic characteristics of the tandem-airfoil system are strongly influenced by airfoil-to-airfoil interference effects arising from the downwash generated by the fore airfoil. The presence of a laminar separation bubble on the suction surface of each airfoil is found to alter the lift and drag coefficients as well as the lift-to-drag ratio. The wake of the fore airfoil is often seen impinging on the aft airfoil, which is a key mechanism by which the lift and drag forces are altered. The gains in aerodynamic efficiency achieved by the tandem airfoils become smaller as the stagger increases owing to reduced airfoil-to-airfoil interference. The effect of ground clearance on the tandem airfoils is found to be similar to that on the isolated airfoil, with both the lift and drag coefficients increasing with decreasing ground clearance. Overall these results provide new insight into the aerodynamics of tandem airfoils at low Reynolds numbers, contributing to the development of the next generation of PAVs for thermal surveillance applications.

1 Introduction

In recent years, uncrewed aerial vehicles (UAVs) have attracted growing interest owing to an expanding array of potential applications, ranging from thermal surveillance to infrastructure inspection. Meanwhile, the dimensions of UAVs have been steadily decreasing, putting us now at the cusp of an era in which pico-aerial vehicles (PAVs) are within reach. According to Wood *et al.* [1], PAVs are defined as having a maximum linear dimension of 5 cm and a maximum take-off mass of 500 mg. Owing to their exceptionally small length and velocity scales, the Reynolds number range of PAVs is estimated to be on the order of 10^2 to 10^3 [1]. Unfortunately, however, knowledge of the aerodynamics of airfoils in this ultra-low *Re* regime is still incomplete, particularly when the airfoils are operating in the vicinity of other surfaces, such as the ground. Nevertheless, previous studies have shown that, under certain conditions, arranging airfoils in a tandem configuration can improve their aerodynamic efficiency, with the stagger distance, gap height and decalage found to have particularly strong effects on the lift and drag characteristics [2]. Other potential areas of interest include aerodynamic noise [3], in-flight icing in clouds of super-cooled droplets [4], and novel propulsion systems based on fuel cells and micro combustors [5−7].

Kurtulus [8] investigated the unsteady flow around a single NACA 0012 airfoil at *Re* = 1000. A sharp discrete peak in the frequency spectrum of the lift coefficient was observed at an angle of attack of α = 8°, indicating the presence of periodic limit-cycle oscillations [8]. Using direct numerical simulations, He *et al.* [9] investigated the effects of slip and no-slip ground surfaces on the stability of separated flow around a NACA 4415 airfoil at low *Re* (300−1000) and a high angle of attack (α = 20°). They found that, depending on its specific type, the ground can produce drastically different effects on the unsteady aerodynamics. For a no-slip ground, decreasing the ground clearance was found to be stabilizing, but this effect weakened with increasing *Re*. In addition, decreasing the ground clearance was also found to decrease the lift and drag coefficients, an effect attributed to the slower flow in the growing boundary layer. For a slip ground, which does not have a boundary layer, the pressure under the airfoil increases with decreasing ground clearance, causing both the lift and drag coefficients to increase. This

study by He *et al.* [9] was later extended to the case of a wavy ground [10] and involving a linear non-modal stability analysis [11].

Fu *et al.* [12] investigated the design parameters of tandem airfoils with NACA 6409 profiles at $Re = 200,000$. They found that the aerodynamic performance was particularly sensitive to the decalage angle and that improved performance can be achieved only when the fore airfoil is higher than the aft airfoil. As the stagger distance increases, the aerodynamic performance increases at first but then saturates owing to weakening interactions between the fore and aft airfoils. Fanjoy *et al.* [13] also investigated tandem-airfoil systems. They found that the drag on the aft airfoil increases as the stagger decreases, with the fore airfoil experiencing an expanded drag bucket and the lift-to-drag ratio increasing. Fature *et al.* [14] examined the turbulent flow around tandem airfoils arranged in a T configuration at high α and moderate *Re*. They examined how the tail lift coefficient depends on the position and width of the airfoil's wake and on the path lines of the shed vortices. They also performed a statistical analysis of the velocity field, focusing on the recirculation zone, wake velocity deficient, wake width, and turbulence level in detached flow. Matyushenko [15] investigated the flow around NACA 0012 airfoils arranged in a tandem configuration and demonstrated the accuracy of different transition models. Scharpf *et al.* [16] performed experiments on FX 63-137 airfoils in a tandem setup at $Re = 85,000$ with a stagger of 1.5 times the chord length (*c*), a gap of 0, and a decalage angle of 0 and $\pm 10°$ [16]. They benchmarked the performance of the tandem airfoils against that of a single airfoil and found, for certain conditions, both an increase in lift and a decrease in total drag, resulting in a significant increase in the lift-to-drag ratio [16].

Using numerical simulations, Kurtulus [17] examined the wake pattern generated by a single symmetric airfoil at $Re = 1000$, with a focus on the effect of the incidence angle and the airfoil's thickness on the formation of alternating vortex patterns. Aerodynamic quantities such as the lift and drag coefficients as well as the lift-to-drag ratio were analyzed alongside the non-dimensional oscillation frequency, the Strouhal number. Five different types of wake patterns were identified based on an analysis of the instantaneous and time-averaged velocity fields. This study by Kurtulus [17] provides helpful insight into the wake patterns generated by a symmetric airfoil at low *Re*. Using

the vortex particle method, Rossi *et al.* [18] numerically investigated sudden changes in the flow field past stalled airfoils and found results consistent with those of Kurtulus [17].

As the foregoing review has shown, despite an abundance of research in the general field of two-dimensional airfoil aerodynamics, there is still limited research on the flow field around two tandem airfoils in ground effect at Reynolds numbers low enough to be relevant to PAVs. In this parametric study, we numerically simulate the low-*Re* flow around a pair of NACA 0012 airfoils arranged in a tandem configuration close to a slip ground surface. We intentionally keep the angle of attack constant at $\alpha = 5^{\mathrm{o}}$ for both the fore and aft airfoils in order to maintain zero decalage effects. We also keep the Reynolds number constant at a value low enough to be relevant to PAVs: $Re = 500$. We allow for ground effect so as to focus on the conditions under which PAVs might operate during take-off and landing. We parametrically examine the effects of stagger distance, gap height and ground clearance on the lift and drag coefficients of the two-tandem-airfoil system, and compare the results against baseline reference values computed for two identical airfoils in isolation (without airfoil-to-airfoil interactions).

The rest of this paper is organized as follows. In §2, we numerically simulate a single airfoil in order to validate our numerical framework against published data. In §3, we present the numerical framework and boundary conditions used in the tandem-airfoil simulations. In §4, we examine the aerodynamic coefficients (lift and drag), velocity contours, vector fields and vorticity contours, as well as the generation of a laminar separation bubble. We then discuss the mechanisms influencing the aerodynamic performance of the tandem airfoils. In §5, we conclude by summarizing the key results and implications of this study.

2 Numerical setup: A single airfoil without ground effect

2.1 Numerical setup

The computational domain for the single-airfoil simulations is shown in Figure 2.1-1. For the case with ground effect (left subfigure), the distance from the trailing edge of the airfoil to the ground surface is defined as the ground clearance. The distance from the leading edge of the airfoil to the left boundary of the domain is $15c$, where c is the chord length of the airfoil. The distance from the leading edge of the airfoil to the right boundary of the domain is $25c$. The height of the entire domain is $20c$. The left boundary is defined as a velocity inlet, the right and top boundaries are defined as pressure outlets, and the bottom boundary (ground) is defined as a slip wall so that no boundary layer can develop on it. However, the airfoil surface itself is defined as a no-slip wall.

For the case without ground effect (right subfigure), the computational domain is a semi-circle with radius $15c$ centered on the airfoil. Appended to the right boundary of this semi-circle is a rectangular subdomain, with a width of $25c$, as shown in the right subfigure of Figure 2.1-1. The semi-circular boundary is defined as a velocity inlet, while the top, bottom and right boundaries are defined as pressure outlets. As before, the airfoil surface itself is defined as a no-slip wall.
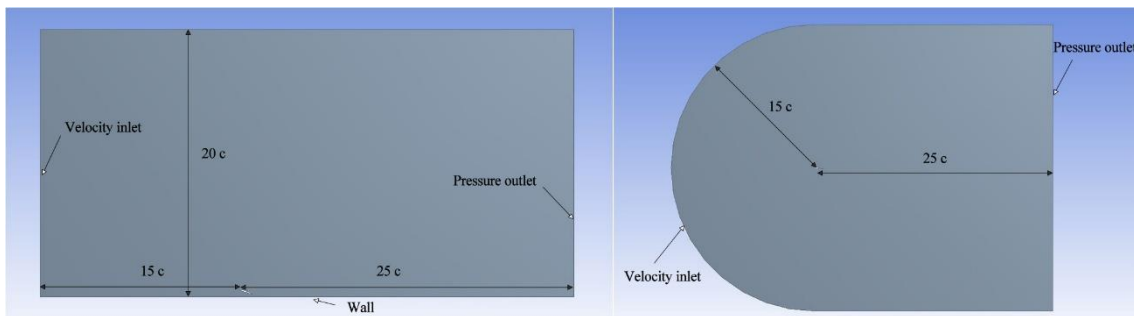

Figure 2.1-1 Computational domain around a single NACA 0012 airfoil (left) with ground effect and (right) without ground effect.

ICEM is used to generate the computational mesh, whose geometrical details are shown in Figure 2.1-2. The first cell spacing of the mesh around the airfoil is set to $0.0015c$ in order to ensure that y+ is smaller than 1.
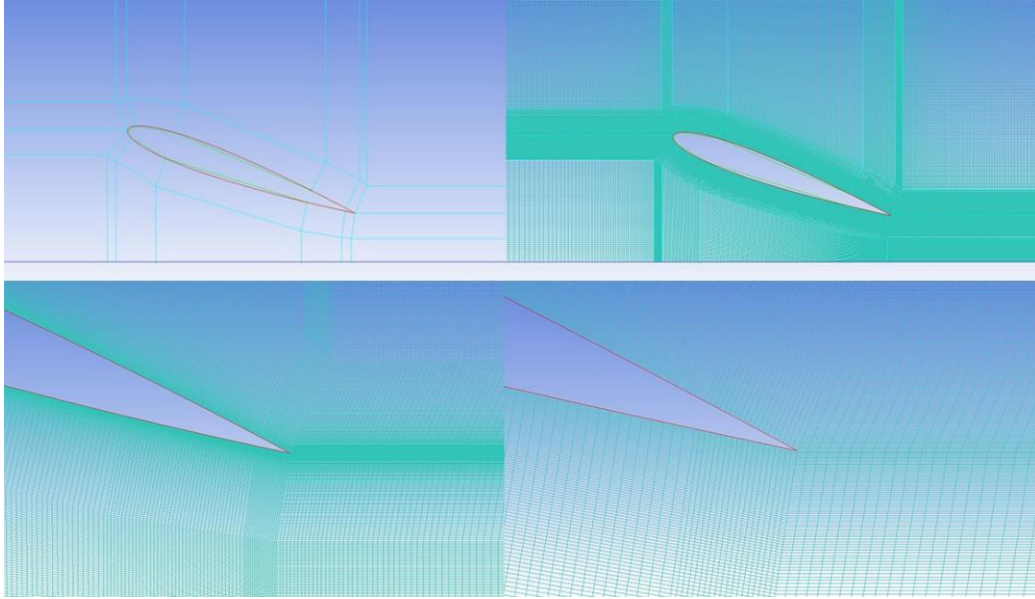
Figure 2.1-2 Computational mesh for the single airfoil test case.

A pressure-based numerical solver built into ANSYS Fluent is used to seek a transient solution. Given the ultra-low Reynolds number (*Re* = 500) of this system, a laminar model is used to numerically simulate the flow in a transient unsteady framework. The fluid medium is air, and its density and dynamic viscosity are both set to their default values. All reference values used for non-dimensionalization are taken at the inlet (left boundary of the domain). Pressure−velocity coupling is used in the flow solver, and the transient formulation is second-order implicit. The input data and settings for these single-airfoil simulations are listed in Table 1.

Table 1 Settings for single-airfoil simulations

Variables	Grid refinement	Data validation
α (°)	20	10 and 11
Chord length (m)	0.05	0.1
First cell spacing	0.0015c	0.0015c
Free-stream velocity (m/s)	0.146	0.146
Solver type	Transient	Transient

2.2 Grid refinement and sensitivity analysis

A grid refinement test is performed at α = 20° and Re = 500 with ground effect (ground clearance, H = 0.2c) and $\triangle t$ = 0.01 s, as shown in Figure 2.2-1. The coarse mesh contains 207,888 elements, the medium mesh contains 251,902 elements, and the fine mesh contains 308,448 elements. It can be seen that, between the fine and medium meshes, the variations in the lift and drag coefficients are relatively small. For the medium mesh, the differences in the time-averaged lift and drag coefficients, relative to those of the fine mesh, are only 0.191% and 1.660%, respectively. These small differences indicate that the medium mesh is sufficiently refined to be able to resolve the flow. Note that both the lift and drag coefficients oscillate periodically in time, suggesting that the flow is undergoing large-scale vortex shedding. This is consistent with the presence of a global self-excited hydrodynamic mode arising from a region of local absolute instability [19]. Such self-excited oscillations are typically characterized by globally synchronized motion at a discrete natural frequency and by relative insensitivity to external perturbations at other frequencies [19]. They can be found in a variety of fluid mechanical systems, such as bluff-body wakes [20], low-density jets [21−29] and jet diffusion flames [30−32]. As an aside, it is worth mentioning that self-excited oscillations can arise not just from hydrodynamic mechanisms (i.e. not just from local absolute instability) but also from other physical mechanisms, such as the coupling between the heat-release-rate oscillations of an unsteady flame and the pressure oscillations of its surrounding acoustic enclosure [33−37]. This type of coupling gives rise to a problem known as thermoacoustic instability [38−39], which must be adequately controlled [40−44] or forecasted [45] if terminal damage to combustion chambers is to be prevented.
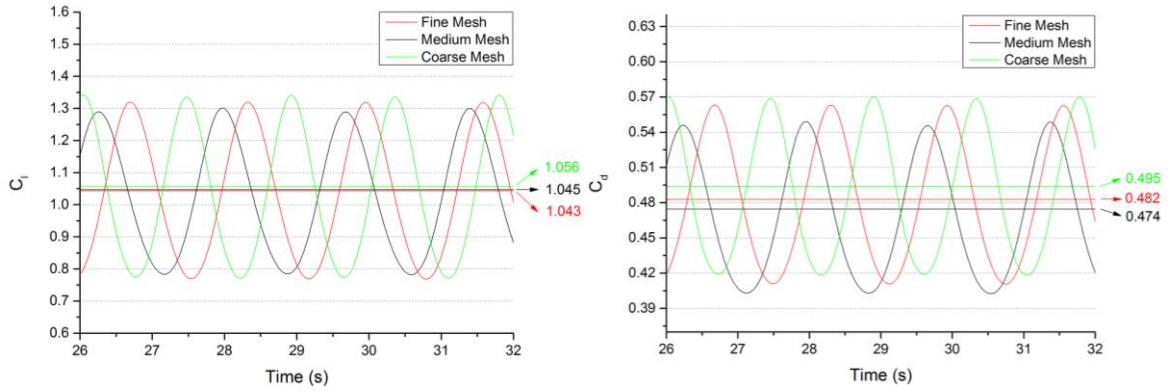
Figure 2.2-1 Grid refinement at α = 20°and *Re* = 500 (26 ≤ *t* ≤ 32 s).

2.3 Data validation

To validate the numerical framework, we benchmark the flow around a single airfoil at α= 10°, 11° and *Re* = 1000 against published data. The time evolution of the lift and drag coefficients are shown in Figure 2.3-1. The time interval $t \in$ [26, 32] is magnified in order to extract the time-averaged value in a regime where the flow has reached a long-time asymptotic state, as shown in Figure 2.3-2. The time-averaged C_l and C_d at α = 10° is 0.396 and 0.162, respectively. The time-averaged C_l and C_d at α = 11° is 0.428 and 0.174, respectively. From these figures, it can be seen that, as expected, the lift coefficient increases with α. These numerical data are sufficiently close to their published values, as evidenced by their errors being consistently below 6%, as shown in Table 2.

Table 2 Data validation at α = 10°, 11° and *Re* = 1000

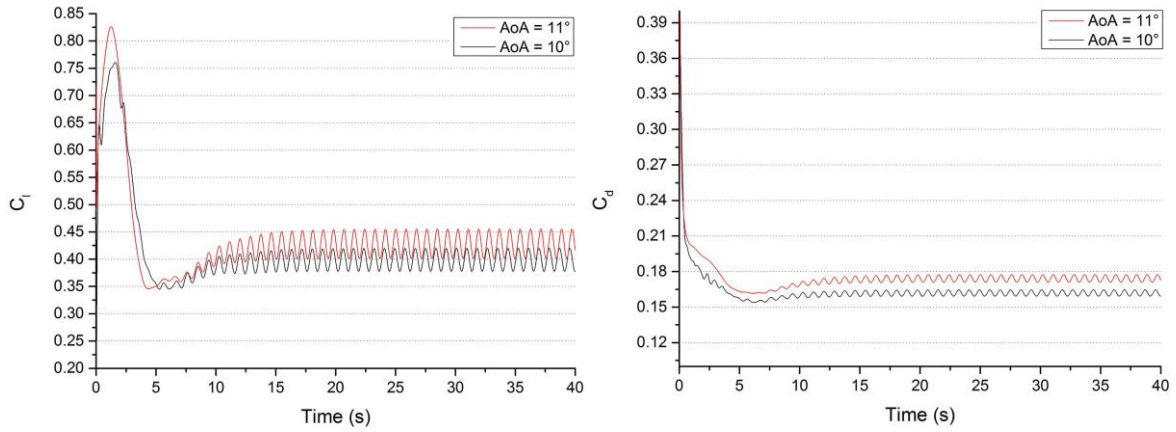| α	Aerodynamic coefficients	Present study	Kurtulus [8]		Liu *et al.* [46]		Khalid *et al.* [47]	
			Value	Error (%)	Value	Error (%)	Value	Error (%)
α = 10°	C_l	0.396	0.410	-3.41	0.420	-5.71	0.392	1.02
	C_d	0.162	0.156	3.85	/	/	/	/
α = 11°	C_l	0.428	0.451	-5.10	0.455	-5.93	0.433	-1.15
	C_d	0.174	0.176	-1.14	/	/	/	/

8

Figure 2.3-1 Full time span: (left) lift and (right) drag coefficients at α = 10°, 11° and *Re* = 1000.

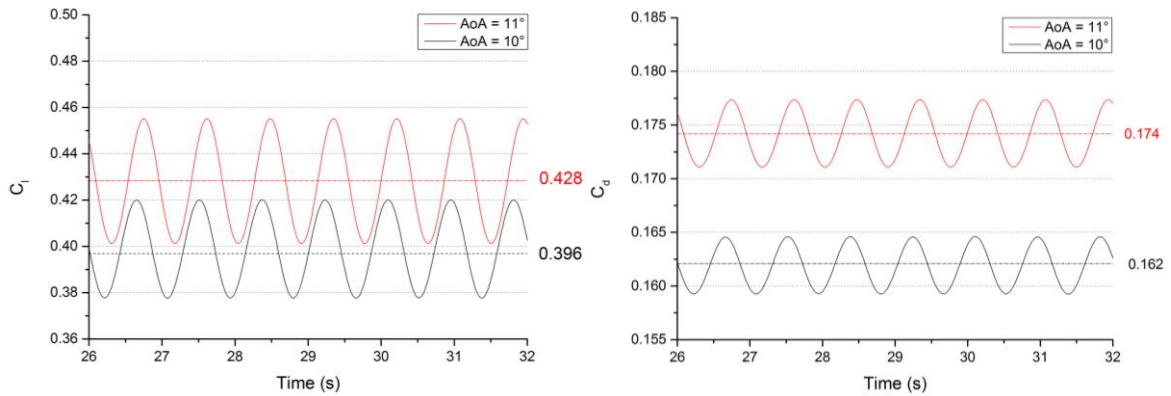**Figure 2.3-2** Selected time window: (left) lift and (right) drag coefficients at α = 10°, 11° and *Re* = 1000.

3 Numerical setup: Two tandem airfoils in ground effect

For the case of two tandem airfoils, we consider both airfoils to have a NACA 0012 profile. For both airfoils, α = 5°, implying that the decalage angle is 0. The Reynolds number is also kept constant at a value low enough to be relevant to PAVs: *Re* = 500. The chord length of the airfoil is *c* = 0.05 m, and the free-stream inlet velocity is 0.146 m/s. The relative positions of the two airfoils above a ground surface are defined by three geometric parameters: the stagger distance (*S*), the gap height (*G*), and the ground clearance (*H*). These parameters are illustrated in Figure 2.3-1. *S* is the horizontal distance between the trailing edge of the fore airfoil and the leading edge of the aft airfoil. *G* is defined as the vertical distance between the trailing edges of the two airfoils,

9

and is positive when the fore airfoil is higher than the aft airfoil (as shown in the example of Figure 2.3-1). *H* is defined as the vertical distance between the trailing edge of the fore airfoil and the ground surface.
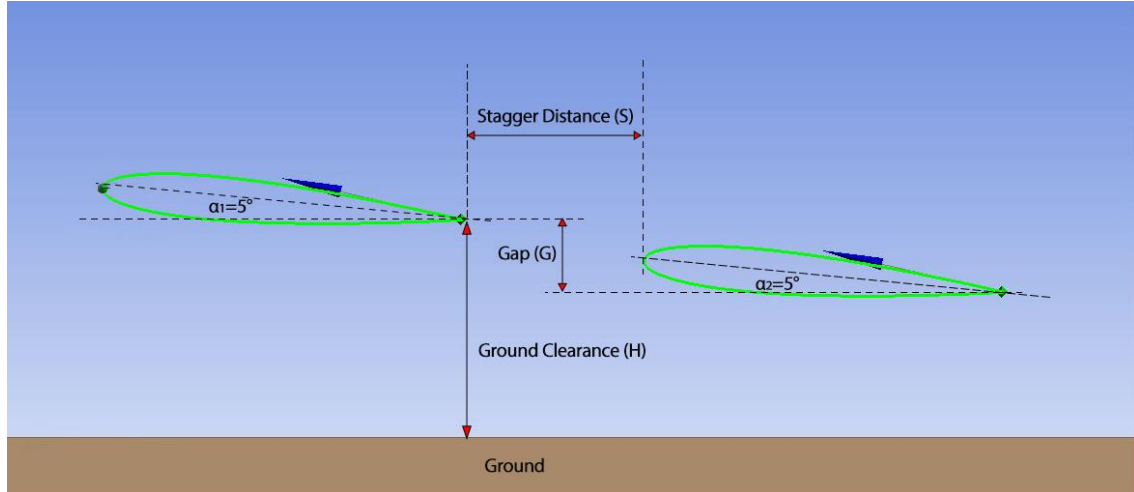

Figure 2.3-1 Geometric parameters defining two tandem airfoils in ground effect.

The computational domain and mesh are shown in Figure 2.3-2. The horizontal distance from the leading edge of the fore airfoil to the left boundary of the domain, which is rectangular in shape, is $15c$, while the horizontal distance from the leading edge of the fore airfoil to the right boundary of the domain is $25c$. The height of the overall domain is $20c$. A velocity inlet boundary condition is imposed on the left boundary of the domain. Pressure outlet boundary conditions are imposed on the top and right boundaries, while a slip wall is imposed on the bottom boundary (ground surface) in order to avoid the formation of a viscous boundary layer there. The airfoil surface itself is defined by a no-slip wall, with a NACA 0012 profile. The details of the computational mesh are shown in Figure 2.3-3. It can be seen that the resolution of the mesh is higher near the airfoil surface so as to resolve the stronger velocity gradients there. There are also more grid cells in the wake of the airfoils, because large-scale vortex shedding is expected to occur there. The computational mesh, created in ICEM, is imported into ANSYS Fluent, where it is solved numerically using the settings listed in Table 3. The angle of attack for both the fore and aft airfoils is fixed at $\alpha = 5^\circ$.
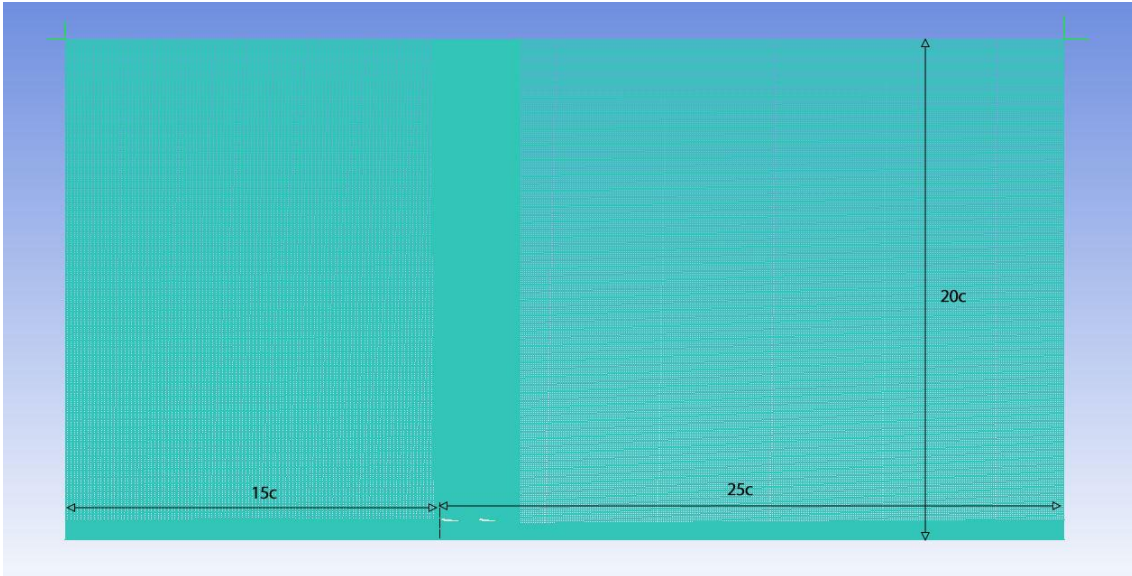
Figure 2.3-2 Computational domain for two tandem NACA 0012 airfoils in ground effect
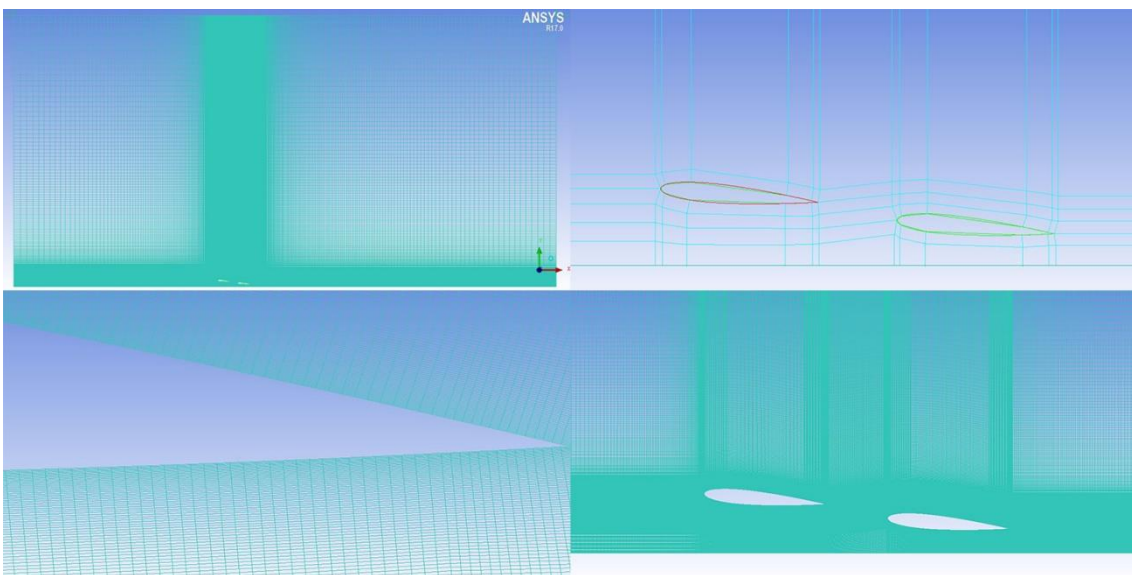

Figure 2.3-3 Detailed view of the computational mesh around two tandem NACA 0012 airfoils in ground effect. The angle of attack for both the fore and aft airfoils is fixed at α = 5°.

Table 3 Settings for tandem-airfoil simulations

Setting	Value
Angle of attack, α (°)	5

Chord length, c (m)	0.05
First cell spacing	$0.0015c$
Viscous model	Laminar
Free-stream velocity (m/s)	0.146
Solver type	Transient
Reynolds number, Re	500

Owing to the large number of parameters that can potentially influence the aerodynamic performance of two tandem airfoils in ground effect, we carry out a parametric study of the key parameters, as is commonly done in numerical investigations of fluid flows [48−52]. We consider a total of 12 test cases, which are listed in Table 4. Test cases 1−5 are designed to enable an investigation of the effect of stagger distance (S). Test cases 6−10 are designed to enable an investigation of the effect of the gap height (G) between the two tandem airfoils. Test cases 1, 9, 11 and 12 are designed to enable an investigation of the effect of ground clearance (H).

Table 4 Summary of the test cases. All length scales are expressed in terms of chord length, c.

Test No.	Stagger distance (c)	Gap (c)	Ground clearance (c)
1	0.5	0.2	0.4
2	0.7	0.2	0.4
3	1	0.2	0.4
4	1.5	0.2	0.4
5	2	0.8	0.6
6	0.5	-0.4	0.6
7	0.5	-0.2	0.6
8	0.5	0	0.6
9	0.5	0.2	0.6
10	0.5	0.4	0.6
11	0.5	0.2	0.8
12	0.5	0.2	1

4 Results and discussion

4.1 Flow around two tandem airfoils in ground effect

To give an overview of the spatiotemporal evolution of the two-dimensional flow field around two tandem airfoils in ground effect, we first present a sample case for which $S = 0.5c$, $G = 0.2c$, $H = 0.4c$, and $Re = 500$.

The spatial distribution of velocity vectors is shown in Figure 4.1-1, from which we can identify the formation of a laminar separation bubble on both airfoils at $t = 4$ s. The flow over the rear portion of both airfoils is subjected to strong adverse pressure gradients, which cause the laminar boundary layer to separate and move away from the airfoil surface. The complex dynamics of the laminar separation bubble can lead to undesirable effects such as flow oscillations due to bubble flapping. The laminar separation bubble of the fore airfoil is always larger than that of the aft airfoil. The corresponding velocity contours are shown in Figure 4.1-2 and corroborate the observations shown by the velocity vector field in Figure 4.1-1.

The corresponding contours of the pressure distribution are shown in Figure 4.1-3. It can be seen that the aerodynamic interaction between the two tandem airfoils has altered the pressure distribution on each airfoil significantly, as compared with the case without any airfoil-to-airfoil interaction. In particular, the pressure on the lower surface of the fore airfoil has increased, giving rise to an increase in lift generation. The pressure distribution around the leading edge on the upper surface of the aft airfoil decreases markedly, as a result of the downwash generated by the fore airfoil. The pressure on the lower surface of the aft airfoil decreases slightly. Overall, these changes in the pressure distribution around the two tandem airfoils at this particular geometric configuration produce a decrease in lift, but this is not always the case for the other geometric configurations, as we will see later. The spatial distribution of vorticity is shown in Figure 4.1-4. It can be seen that the vorticity distribution differs significantly between the two tandem airfoils, leading to different flow separation and lift generation characteristics. The flow is mostly attached to the airfoil, especially over the pressure surface, with no evidence of large-scale vortex shedding at this particular combination of stagger distance, gap height, ground clearance, and Reynolds number.
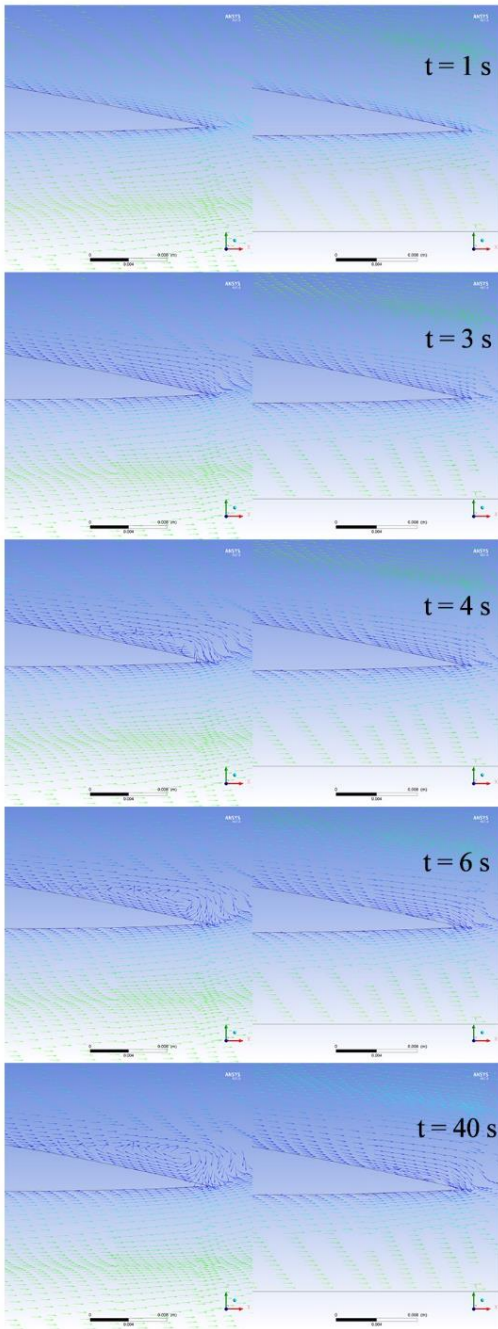
Figure 4.1-1 Laminar separation bubble on two tandem airfoils (left: fore airfoil, right: aft airfoil) at $Re = 500$, $S = 0.5c$, $H = 0.4c$, and $G = 0.2c$.
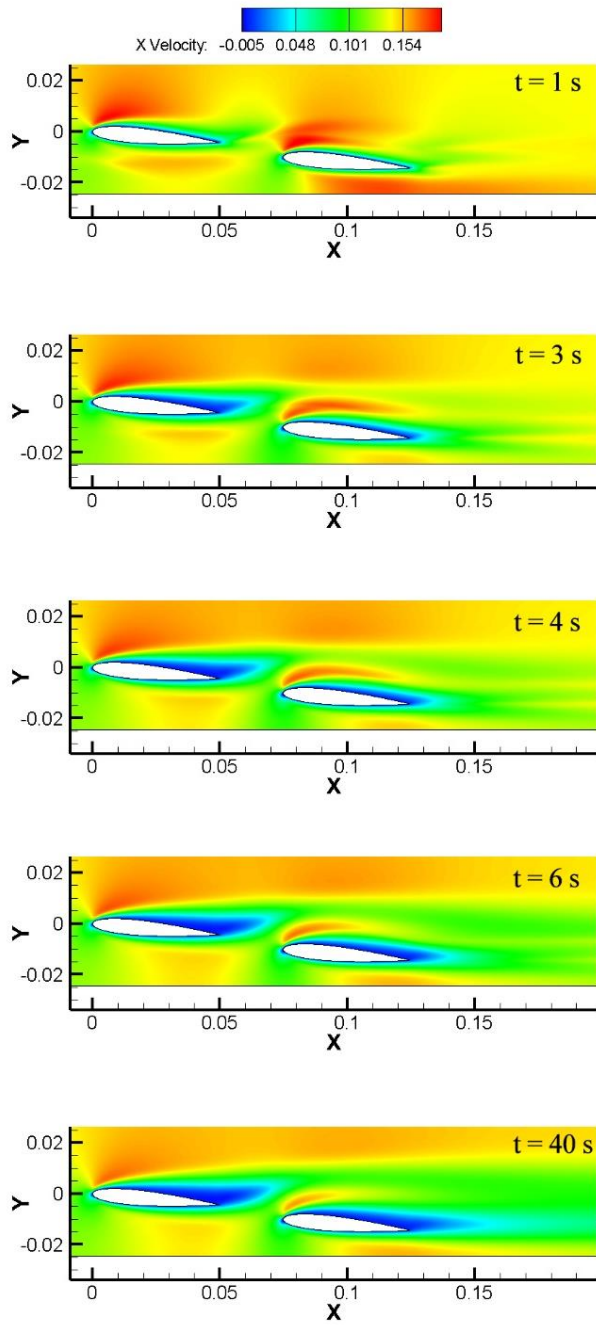
Figure 4.1-2 Velocity contours for flow around two tandem airfoils at $Re = 500$, $S = 0.5c$, $H = 0.4c$, and $G = 0.2c$.
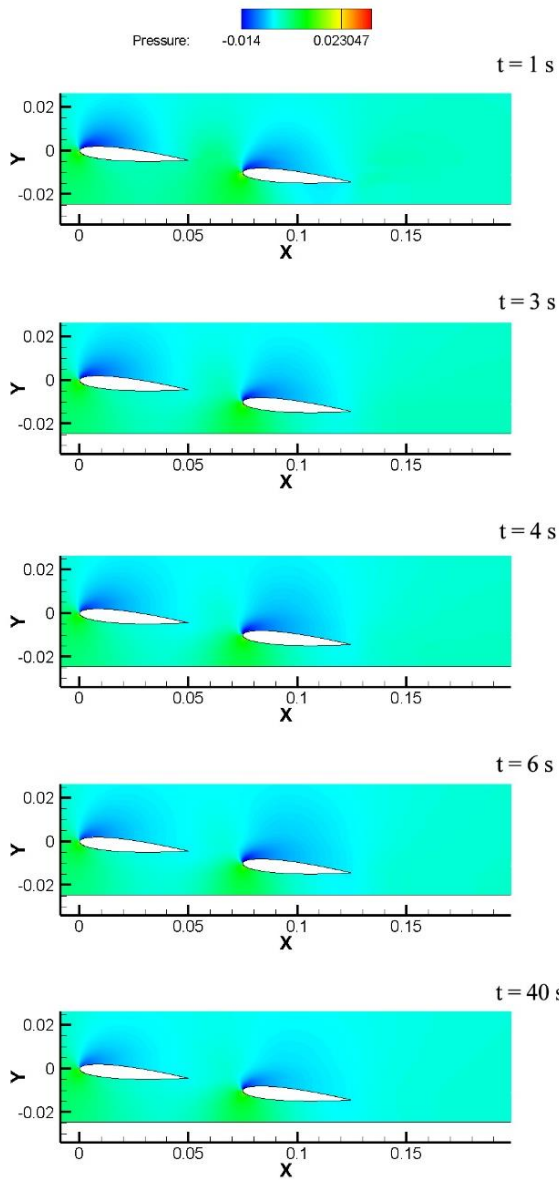
Figure 4.1-3 Pressure contours for flow around two tandem airfoils at $Re = 500$, $S = 0.5c$, $H = 0.4c$, and $G = 0.2c$.
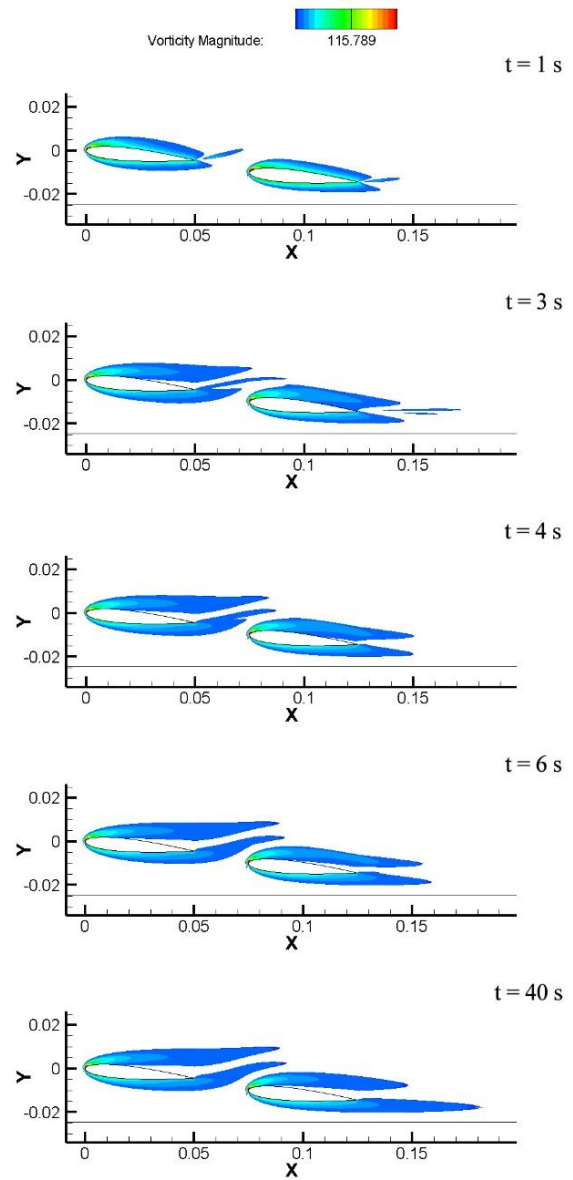
Figure 4.1-4 Vorticity contours for flow around two tandem airfoils at $Re = 500$, $S = 0.5c$, $H = 0.4c$, and $G = 0.2c$.

4.2 Reference data: No airfoil-to-airfoil interaction

To isolate the effects of airfoil-to-airfoil interaction in the two tandem airfoils, we benchmark the tandem-airfoil data against reference data computed for the flow around the same two airfoils, but when they are isolated from each other (i.e. without airfoil-to-airfoil interaction).

To acquire the reference data, we numerically simulate the two-dimensional flow around single isolated airfoils in turn, at identical values of the Reynolds number, angle of attack, and ground clearance so as to have a representative baseline. The reference data for the fore airfoil refer to the aerodynamic coefficients (lift and drag) of an isolated airfoil with the same ground clearance as the fore airfoil of the tandem configuration. Similarly, the reference data for the aft airfoil refer to the aerodynamic coefficients (lift and drag) of an isolated airfoil with the same ground clearance as the aft airfoil of the tandem configuration. The mean reference values of the tandem configuration refer to the average aerodynamic coefficients (lift and drag) between (i) an isolated airfoil with the same ground clearance as the fore airfoil of the tandem configuration and (ii) an isolated airfoil with the same ground clearance as the aft airfoil of the tandem configuration.

In the reference configuration, the aerodynamic coefficients for lift and drag are defined as follows:

$$C_{l(reference)} = \frac{C_{l(single\ fore)} + C_{l(single\ aft)}}{2} \tag{4-1}$$

$$C_{d(reference)} = \frac{C_{d(single\ fore)} + C_{d(single\ aft)}}{2} \tag{4-2}$$

In the tandem configuration, the aerodynamic coefficients for lift and drag are defined as follows:

$$C_{l(tandem)} = \frac{C_{l(fore)} + C_{l(aft)}}{2} \tag{4-3}$$

$$C_{d(tandem)} = \frac{C_{d(fore)} + C_{d(aft)}}{2} \tag{4-4}$$

4.3 Effect of gap height

First we examine the effect of the gap height between two tandem airfoils at $S = 0.5c$ and $H = 0.6c$. The lift and drag coefficients are plotted in Figure 4.3-1 as a function of the gap height, G. From these figures, we can examine how the lift and drag coefficients, as well as the lift-to-drag ratio, vary with G.
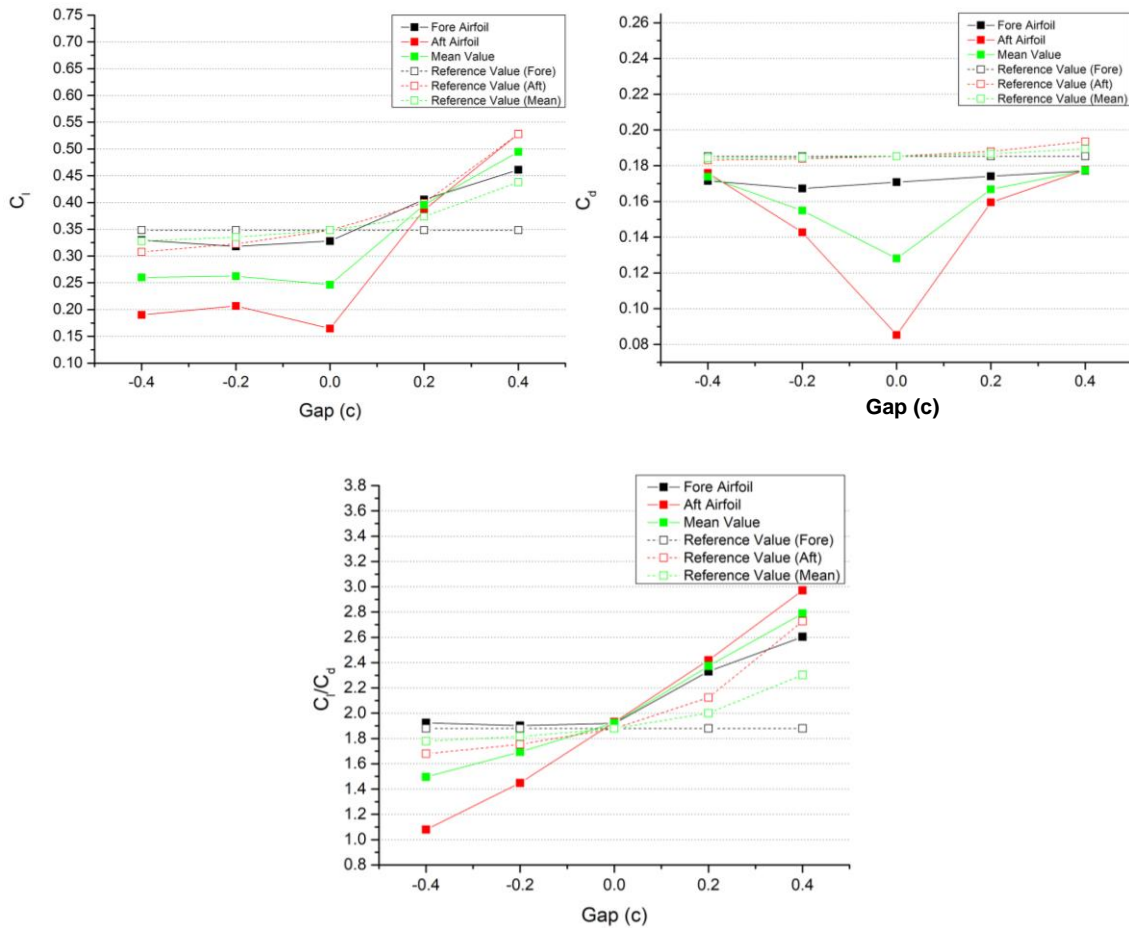

Figure 4.3-1 (top) Lift coefficient, (middle) drag coefficient, and (bottom) lift-to-drag ratio as a function of the gap height at $Re = 500$, $S = 0.5c$, and $H = 0.6c$.

From Figure 4.3-1, it can be seen that both the lift and drag coefficients of the aft airfoil are markedly lower than those of the corresponding reference values. For both the lift and drag coefficients, there exists a "bucket" when $G = 0$. However, when G is positive, the lift coefficient of the aft airfoil increases to a higher value, but it remains less than the corresponding reference value. The aerodynamic coefficients of the fore airfoil do not vary as much as those of the aft airfoil, which is to be expected because the fore

airfoil always experiences a uniform free-stream velocity, whereas the aft airfoil is affected by the wake of the fore airfoil. In particular, when G is small, the wake from the fore airfoil impinges more or less directly on the aft airfoil, affecting its aerodynamic loads. The downwash from the fore airfoil causes the aft airfoil to operate at a lower local angle of attack, decreasing the effective angle of attack of the aft airfoil and thus reducing lift. Because the low-momentum flow in the wake of the fore airfoil passes over the aft airfoil, the local angle of attack is decreased, with the effective velocity deficient in the wake reducing the drag force acting on the aft airfoil. The maximum reduction in drag occurs when the center of the wake directly impinges on the leading edge of the aft airfoil. This is believed to be the physical cause of the "bucket" observed in the drag-coefficient curve. The presence of the aft airfoil makes the flow over the fore airfoil slightly more prone to separation, leading to slightly lower lift and drag coefficients. In addition, the resulting lift coefficient of the aft airfoil is also smaller in magnitude. When G is positive, the lift coefficient increases quickly because of the ground effect. When G is large, which means that the ground clearance of the aft airfoil is relatively small, the corresponding lift coefficient becomes larger because of the additional contribution arising from ground effect.

Furthermore, it can be seen that the lift-to-drag ratio increases with increasing G, which is mainly due to the increase of the lift coefficient of the aft airfoil. When G is positive, the lift-to-drag ratio of the aft airfoil is significantly higher than that of the corresponding reference value. This indicates that the aerodynamic characteristics of the aft airfoil in the tandem configuration are better than those of the corresponding single isolated airfoil. These results are in stark contrast to those observed when G is negative.

It is also apparent that the lift-coefficient curve of the fore airfoil becomes roughly constant when G is negative, but starts to increase when G rises above 0, while the drag-coefficient curve of the fore airfoil remains relatively unchanged. The lift-to-drag ratio of the fore airfoil starts to increase when G is positive, which is similar to the behavior observed in the aft airfoil but here the slope is higher, which suggests that the aerodynamic airfoil-to-airfoil interaction has a stronger effect on the aft airfoil than it does on the fore airfoil.

Regarding the mean lift and drag coefficients, there still exists a "bucket" but it is more apparent in the drag coefficient than it is in the lift coefficient. The mean lift-to-drag ratio continues to increase regardless of whether G is positive or negative, but it remains consistently higher than its corresponding reference value. Moreover, the increase in the mean lift-to-drag ratio is larger when G is positive, which, as we will see later, can be attributed to the ground effect. In summary, these results show that two tandem airfoils have better aerodynamic performance than two single airfoils in isolation.

4.4 Effect of stagger distance

According to the previous section, the aerodynamic performance of two tandem airfoils, quantified by their lift-to-drag ratio, tends to improve when the gap height becomes positive and large. Consequently, a positive and large value of G is used here to examine the effect of stagger distance. We examine the numerical results for different S values at $G = 0.2c$ and a fixed ground clearance of $H = 0.4c$. The lift and drag coefficients, along with the lift-to-drag ratio, are plotted in Figure 4.4-1 as a function of S. From these figures, we can examine how the lift and drag coefficients and the lift-to-drag ratio vary with S.
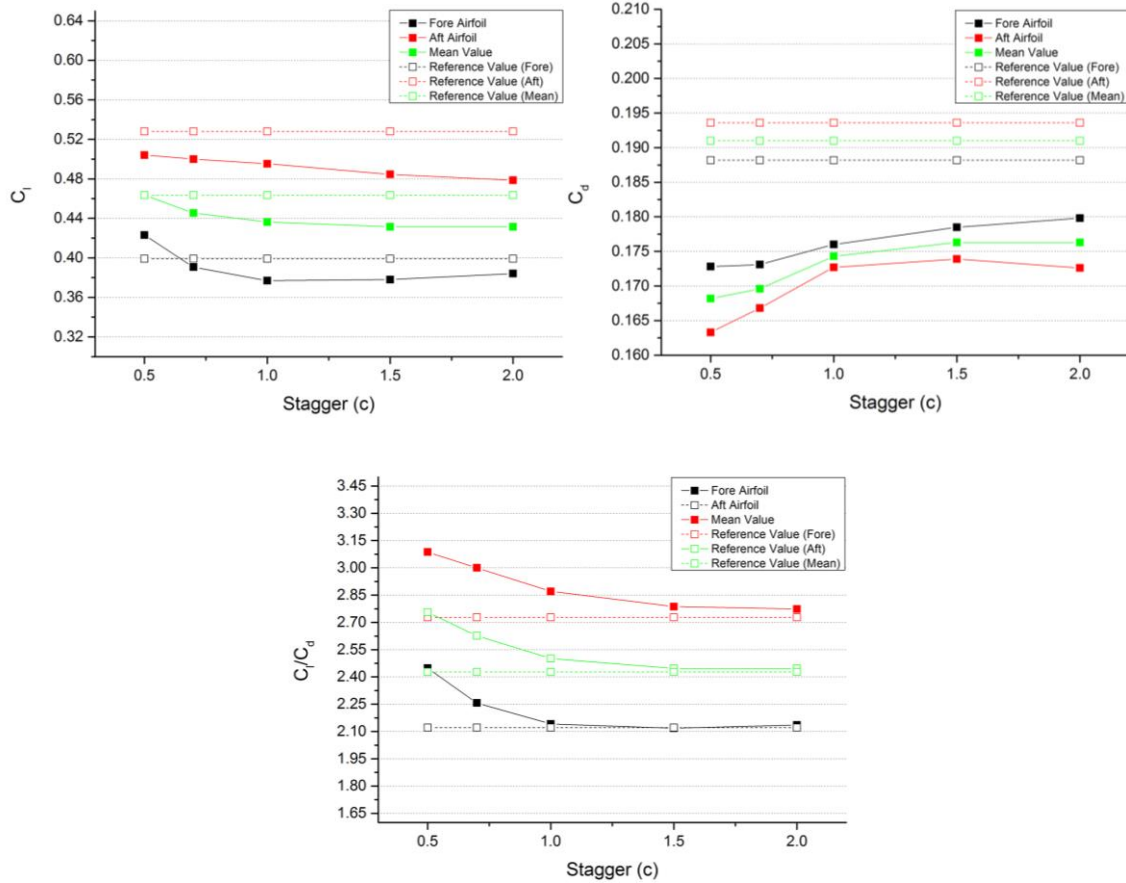
Figure 4.4-1 (top) Lift coefficient, (middle) drag coefficient, and (bottom) lift-to-drag ratio as a function of the stagger distance at $Re = 500$, $G = 0.2c$, and $H = 0.4c$.

From Figure 4.4-1, it can be seen that the lift coefficients of both the fore and aft airfoils of the tandem configuration decrease as S increases. This is physically due to a weakening of airfoil-to-airfoil interference effects as S increases. It should be noted that when $S = 0.5c$, the lift coefficient of the fore airfoil is higher than the corresponding reference value. With the exception of this specific condition, all other data points for a single airfoil in the tandem configuration are lower than the reference values. This is because the length of the laminar separation bubble here is shorter than that in the corresponding reference airfoil, as illustrated in Figure 4.4-2. Such flow separation decreases lift and increases drag, impairing the aerodynamic performance of these tandem airfoils. The resultant mean lift coefficient also decreases with increasing S and is lower than the reference value, except for $S = 0.5c$ when both the tandem configuration and the reference value take on approximately the same lift coefficient

because the decrease in the lift coefficient of the aft airfoil is balanced by the increase in the lift coefficient of the fore airfoil.
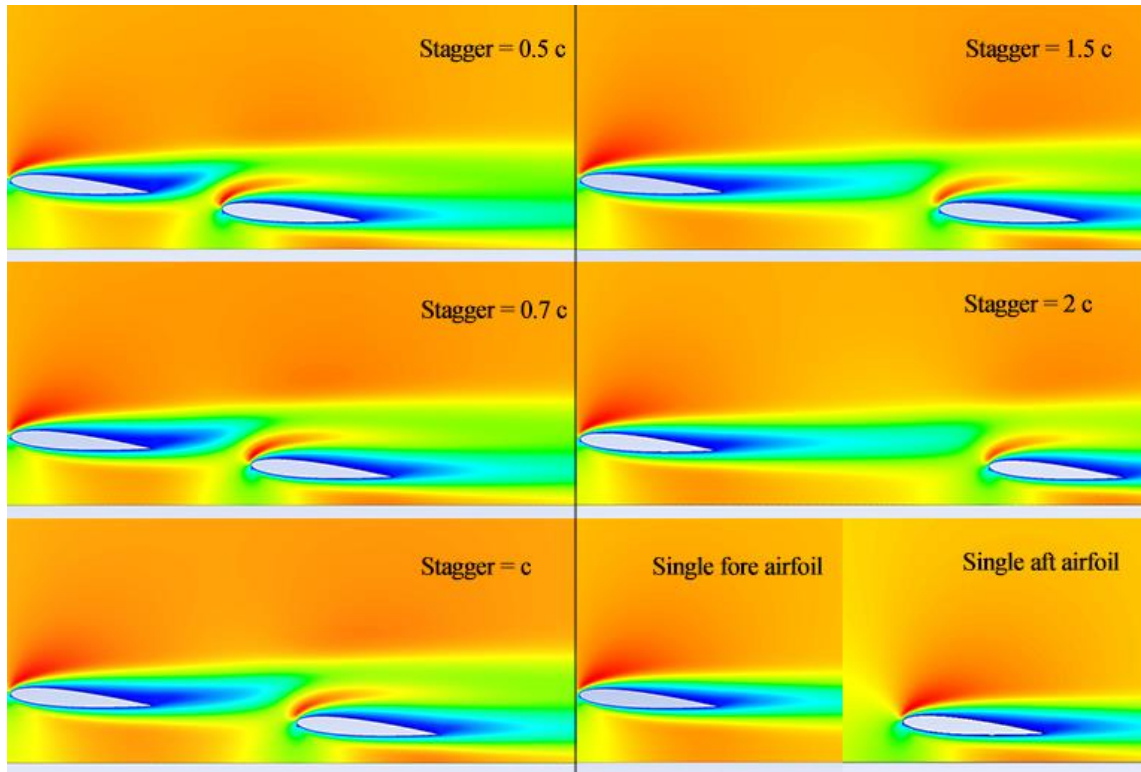

Figure 4.4-2 Velocity contours for two tandem airfoils at different values of stagger ($t = 60$ s).

The drag coefficient of the fore airfoil continues to increase with increasing S, although this increase becomes less strong when S is large because the airfoil-to-airfoil interaction effect arising from the two tandem airfoils decreases. The drag coefficient of the aft airfoil increases and then decreases slightly, while the mean drag coefficient increases first but then remains relatively constant.

It can be seen that the lift-to-drag ratios for both the fore and aft airfoils, as well as the mean lift-to-drag ratio, decrease with increasing S, but are still higher than the corresponding reference values. Nevertheless, these values are closer to the reference values when S is large because that is when the aerodynamic interaction between the two tandem airfoils is relatively weak. When the two tandem airfoils are positioned away from each other, the aerodynamic interference between them weakens.

4.5 Effect of ground clearance

From the analysis presented in §4.3 (Effect of gap height) and §4.4 (Effect of stagger distance), it is clear that a tandem configuration with a large positive gap height and a small stagger distance is beneficial for aerodynamic performance, as determined by a high lift-to-drag ratio. Here we examine the effect of ground clearance (H) at $G = 0.2c$, $S = 0.5c$, and $Re = 500$. The lift and drag coefficients, as well as the lift-to-drag ratio, are plotted in Figure 4.5-1 as a function of H. From these figures, we can examine how the lift and drag coefficients and the lift-to-drag ratio vary with H.
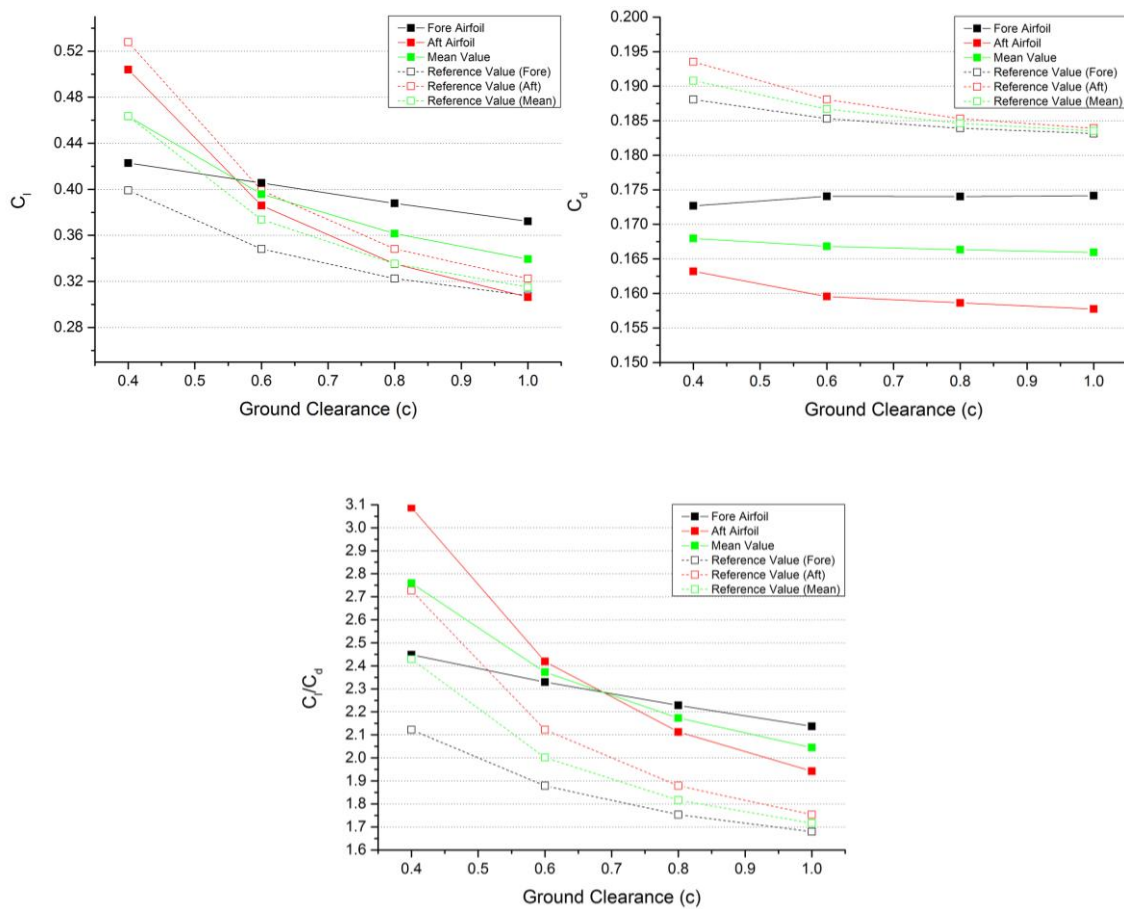
Figure 4.5-1 (top) Lift coefficient, (middle) drag coefficient, and (bottom) lift-to-drag ratio as a function of the ground clearance at $Re = 500$, $G = 0.2c$, and $S = 0.5c$.

From Figure 4.5-1, it can be seen that the lift coefficient of the fore airfoil decreases more or less linearly with increasing H. Furthermore, its value is always higher than the reference value. By contrast, the lift coefficient of the aft airfoil is always lower than the reference value. It decreases rapidly at first and then more gradually as H increases,

indicating a weakened influence when the two tandem airfoils are positioned farther away from the ground surface. The mean lift coefficient is similar to that of the aft airfoil because of the greater decrease attributed to the aft airfoil.

The aerodynamic interference between the two tandem airfoils is seen to change the pressure distribution around each airfoil (not shown here for brevity). Specifically, the pressure on the suction surface decreases, contributing to an increase in lift for the fore airfoil. The pressure distribution at the leading edge on the suction surface of the aft airfoil increases significantly as a result of the downwash generated by the fore airfoil. By contrast, the pressure on the bottom surface of the airfoil increases only slightly. Consequently, these changes in the pressure distribution around the aft airfoil give rise to a decrease in lift.

It can be seen that the drag coefficient is relatively constant compared with the lift coefficient. The drag coefficient of the fore airfoil increases slightly and then remains relatively constant at around $H = 0.6c$. By contrast, the drag coefficient of the aft airfoil decreases slightly with increasing H. These two trends counteract each other to produce a resultant mean drag coefficient that remains roughly constant, despite variations in H.

All the lift-to-drag ratios decrease with increasing H, albeit at different slopes. These ratios decrease because, as H increases, the airfoils move farther away from the ground, reducing the ground effect. All the lift-to-drag-ratio curves for the two tandem airfoils are consistently higher than their corresponding reference values, which indicates again that the tandem configuration with aerodynamic interference between the two airfoils is more aerodynamically efficient than the corresponding single isolated airfoils.

5 Conclusions

The proliferation of industrial and consumer applications for PAVs has necessitated a better understanding of the flow field around airfoils at low Re and in ground effect. Previous studies at higher Re have shown that arranging two airfoils in a tandem configuration can lead to improved aerodynamic performance (i.e. a higher lift-to-drag ratio) than two identical airfoils in isolation. In this parametric study, we numerically simulate the two-dimensional flow field around two NACA 0012 airfoils arranged in a

tandem configuration above a flat ground surface at $Re = 500$. We consider the effects of stagger distance, gap height and ground clearance on the aerodynamic performance, as quantified by the lift and drag coefficients as well as the lift-to-drag ratio. We benchmark the results against reference values computed for the configuration in which airfoil-to-airfoil interactions are absent.

The results show that, at almost all operating conditions, the two tandem airfoils have higher lift-to-drag ratios than the reference configuration involving isolated airfoils (no airfoil-to-airfoil interaction). The aerodynamic performance of the tandem airfoils improves as the gap height increases, particularly to positive values (i.e. when the fore airfoil is higher than the aft airfoil). The aerodynamic performance of each airfoil in the tandem configuration also changes accordingly because of the airfoil-to-airfoil interactions that lead to a change in the pressure distribution. These interactions also influence the laminar separation bubbles generated on the airfoils, as well as their positions on the suction surface of each airfoil in the tandem configuration. The aerodynamic performance of the tandem airfoils is worst when $G = 0$ because of the influence of the wake and downwash from the fore airfoil. This leads to the formation of a "bucket" in the drag-coefficient curve. The lift-to-drag ratio tends to be smaller and less variable when H increases because the effect of the ground diminishes as the airfoils move farther away from the ground surface. The increase in lift-to-drag ratio of the tandem configuration becomes more gradual with increasing S because of a reduction in the strength of the aerodynamic interaction between the two airfoils. Overall this study has shown that two airfoils arranged in a tandem configuration can be more aerodynamically efficient than two identical airfoils in insolation. When combined with the data provided in this paper, this knowledge can be used to aid the development of the next generation of PAVs, e.g. in thermal surveillance applications.

References

[1] Wood, R.J., Finio, B., Karpelson, M., Ma, K., Pérez-Arancibia, N.O., Sreetharan, P.S., Tanaka, H. and Whitney, J.P., 2012. Progress on 'pico'air vehicles. The International Journal of Robotics Research, 31(11), pp.1292-1302.

[2] Chen, F., Yu, J. and Mei, Y., 2018. Aerodynamic design optimization for low Reynolds tandem airfoil. Proceedings of the Institution of Mechanical Engineers, Part G: Journal of Aerospace Engineering, 232(6), pp.1047-1062.

[3] Yuan, Y., Xu, K. and Zhao, K., 2019. Numerical analysis of transport in porous media to reduce aerodynamic noise past a circular cylinder by application of porous foam. Journal of Thermal Analysis and Calorimetry, pp.1-12.

[4] Deng, H., Chang, S. and Song, M., 2019. Numerical investigation on the performance and anti-freezing design verification of atomization equipment in an icing cloud simulation system. Journal of Thermal Analysis and Calorimetry, pp.1-13.

[5] Majid, N.A., Idris, A.C., Faizal, H.M., Rahman, M.R.A. and Hosseini, S.E., 2019. Characteristics of liquid fuel combustion in a novel miniature vortex combustor. Journal of Thermal Analysis and Calorimetry, pp.1-10.

[6] Pourali, M., Abolfazli Esfahani, J., Fanaee, S.A. and Kim, K.C., 2020. Developing mathematical modeling of the heat and mass transfer in a planar micro-combustor with detailed reaction mechanisms. Journal of Thermal Analysis and Calorimetry, pp.1-16.

[7] Esfe, M.H. and Afrand, M., 2019. A review on fuel cell types and the application of nanofluid in their cooling. Journal of Thermal Analysis and Calorimetry, pp.1-22.

[8] Kurtulus, D.F. (2015). On the unsteady behavior of the flow around NACA 0012 airfoil with steady external conditions at Re = 1000. International Journal of Micro Air Vehicles, 7(3), 301-326.

[9] He, W., Yu, P. and Li, L.K.B., 2018. Ground effects on the stability of separated flow around a NACA 4415 airfoil at low Reynolds numbers. Aerospace Science and Technology, 72, pp.63-76.

[10] He, W., Guan, Y., Theofilis, V. and Li, L.K.B., 2019. Stability of low-Reynolds-number separated flow around an airfoil near a wavy ground. AIAA Journal, 57(1), pp.29-34.

[11] He, W., Pérez, J.M., Yu, P. and Li, L.K.B., 2019. Non-modal stability analysis of low-Re separated flow around a NACA 4415 airfoil in ground effect. Aerospace Science and Technology, 92, pp.269-279.

[12] Fu, J., Ji, S. and Huang, X., 2016. The effects of design parameters on tandem-airfoil configuration aerodynamics. In The 2016 Asia-Pacific International Symposium on Aerospace Technology.

[13] Fanjoy, D.W. and Dorney, D.J., 1996. Numerical simulations of tandem-airfoil aerodynamics (No. 961295). SAE Technical Paper.

[14] Faure, T.M., Hétru, L. and Montagnier, O., 2017. Aerodynamic features of a two-airfoil arrangement. Experiments in Fluids, 58(10), p.146.

[15] Matyushenko, A.A., Stabnikov, A.S. and Garbaruk, A.V., 2018, June. Comparative analysis of transition models in prediction of flow over NACA-0012 airfoils in tandem. In Journal of Physics: Conference Series (Vol. 1038, No. 1, p. 012130). IOP Publishing.

[16] Scharpf, D.F. and Mueller, T.J., 1992. Experimental study of a low Reynolds number tandem airfoil configuration. Journal of Aircraft, 29(2), pp.231-236.

[17] Kurtulus, D.F., 2016. On the wake pattern of symmetric airfoils for different incidence angles at Re=1000. International Journal of Micro Air Vehicles, 8(2), pp.109-139.

[18] Rossi, E., Colagrossi, A., Oger, G. and Le Touzé, D., 2018. Multiple bifurcations of the flow over stalled airfoils when changing the Reynolds number. Journal of Fluid Mechanics, 846, pp.356-391.

[19] Huerre, P. and Monkewitz, P.A., 1990. Local and global instabilities in spatially developing flows. Annual review of fluid mechanics, 22(1), pp.473-537.

[20] Provansal, M., Mathis, C. and Boyer, L., 1987. Bénard-von Kármán instability: transient and forced regimes. Journal of Fluid Mechanics, 182, pp.1-22.

[21] Zhu, Y., Gupta, V. and Li, L.K.B., 2019. Coherence resonance in low-density jets. Journal of Fluid Mechanics, 881.

[22] Kyle, D.M. and Sreenivasan, K.R., 1993. The instability and breakdown of a round variable-density jet. Journal of Fluid Mechanics, 249, pp.619-664.

[23] Murugesan, M., Zhu, Y. and Li, L.K.B., 2019. Complex network analysis of forced synchronization in a hydrodynamically self-excited jet. International Journal of Heat and Fluid Flow, 76, pp.14-25.

[24] Lee, M., Zhu, Y., Li, L.K.B. and Gupta, V., 2019. System identification of a low-density jet via its noise-induced dynamics. Journal of Fluid Mechanics, 862, pp.200-215.

[25] Monkewitz, P.A., Bechert, D.W., Barsikow, B. and Lehmann, B., 1990. Self-excited oscillations and mixing in a heated round jet. Journal of Fluid Mechanics, 213, pp.611-639.

[26] Raghu, S. and Monkewitz, P.A., 1991. The bifurcation of a hot round jet to limit-cycle oscillations. Physics of Fluids A: Fluid Dynamics, 3(4), pp.501-503.

[27] Zhu, Y., Gupta, V. and Li, L.K.B., 2017. Onset of global instability in low-density jets. Journal of Fluid Mechanics, 828.

[28] Li, L.K.B. and Juniper, M.P., 2013. Phase trapping and slipping in a forced hydrodynamically self-excited jet. Journal of Fluid Mechanics, 735.

[29] Li, L.K.B. and Juniper, M.P., 2013. Lock-in and quasiperiodicity in a forced hydrodynamically self-excited jet. Journal of Fluid Mechanics, 726, pp.624-655.

[30] Juniper, M.P., Li, L.K.B. and Nichols, J.W., 2009. Forcing of self-excited round jet diffusion flames. Proceedings of the Combustion Institute, 32(1), pp.1191-1198.

[31] Li, L.K.B. and Juniper, M.P., 2013. Lock-in and quasiperiodicity in hydrodynamically self-excited flames: Experiments and modelling. Proceedings of the Combustion Institute, 34(1), pp.947-954.

[32] Li, L.K.B., 2012. Forcing of globally unstable jets and flames (PhD thesis, University of Cambridge).

[33] Moon, K., Guan, Y., Li, L.K.B. and Kim, K.T., 2020. Mutual synchronization of two flame-driven thermoacoustic oscillators: Dissipative and time-delayed coupling effects. Chaos: An Interdisciplinary Journal of Nonlinear Science, 30(2), p.023110.

[34] Jegal, H., Moon, K., Gu, J., Li, L.K.B. and Kim, K.T., 2019. Mutual synchronization of two lean-premixed gas turbine combustors: Phase locking and amplitude death. Combustion and Flame, 206, pp.424-437.

[35] Guan, Y., Li, L.K.B., Ahn, B. and Kim, K.T., 2019. Chaos, synchronization, and desynchronization in a liquid-fueled diffusion-flame combustor with an intrinsic hydrodynamic mode. Chaos: An Interdisciplinary Journal of Nonlinear Science, 29(5), p.053124.

[36] Guan, Y., Liu, P., Jin, B., Gupta, V. and Li, L.K.B., 2018. Nonlinear time-series analysis of thermoacoustic oscillations in a solid rocket motor. Experimental Thermal and Fluid Science, 98, pp.217-226.

[37] Lee, C.Y., Li, L.K.B., Juniper, M.P. and Cant, R.S., 2016. Nonlinear hydrodynamic and thermoacoustic oscillations of a bluff-body stabilised turbulent premixed flame. Combustion Theory and Modelling, 20(1), pp.131-153.

[38] Balusamy, S., Li, L.K.B., Han, Z., Juniper, M.P. and Hochgreb, S., 2015. Nonlinear dynamics of a self-excited thermoacoustic system subjected to acoustic forcing. Proceedings of the Combustion Institute, 35(3), pp.3229-3236.

[39] Balusamy, S., Li, L.K.B., Han, Z. and Hochgreb, S., 2017. Extracting flame describing functions in the presence of self-excited thermoacoustic oscillations. Proceedings of the Combustion Institute, 36(3), pp.3851-3861.

[40] Guan, Y., Gupta, V., Wan, M. and Li, L.K.B., 2019. Forced synchronization of quasiperiodic oscillations in a thermoacoustic system. Journal of Fluid Mechanics, 879, pp.390-421.

[41] Rigas, G., Jamieson, N.P., Li, L.K.B. and Juniper, M.P., 2016. Experimental sensitivity analysis and control of thermoacoustic systems. Journal of Fluid Mechanics, 787.

[42] Kashinath, K., Li, L.K.B. and Juniper, M.P., 2018. Forced synchronization of periodic and aperiodic thermoacoustic oscillations: lock-in, bifurcations and open-loop control. Journal of Fluid Mechanics, 838, pp.690-714.

[43] Guan, Y., Murugesan, M. and Li, L.K.B., 2018. Strange nonchaotic and chaotic attractors in a self-excited thermoacoustic oscillator subjected to external periodic forcing. Chaos: An Interdisciplinary Journal of Nonlinear Science, 28(9), p.093109.

[44] Guan, Y., Gupta, V., Kashinath, K. and Li, L.K.B., 2019. Open-loop control of periodic thermoacoustic oscillations: experiments and low-order modelling in a synchronization framework. Proceedings of the Combustion Institute, 37(4), pp.5315-5323.

[45] Lee, M., Guan, Y., Gupta, V. and Li, L.K.B., 2020. Input-output system identification of a thermoacoustic oscillator near a Hopf bifurcation using only fixed-point data. Physical Review E, 101(1), p.013102.

[46] Liu, Y., Li, K., Zhang, J., Wang, H., & Liu, L. (2012). Numerical bifurcation analysis of static stall of airfoil and dynamic stall under unsteady perturbation. Communications in Nonlinear Science and Numerical Simulation, 17(8), 3427-3434.

[47] Khalid, M.S.U., and Imran A. Characteristics of flow past a symmetric airfoil at low Reynolds number: A nonlinear perspective. ASME 2012 International Mechanical Engineering Congress and Exposition. American Society of Mechanical Engineers, 2012.

[48] Asadi, A., Kadijani, O.N., Doranehgard, M.H., Bozorg, M.V., Xiong, Q., Shadloo, M.S. and Li, L.K.B., 2020. Numerical study on the application of biodiesel and bioethanol in a multiple injection diesel engine. Renewable Energy, 150, pp.1019-1029.

[49] Yu, P., Lu, R., He, W. and Li, L.K.B., 2018. Steady flow around an inclined torus at low Reynolds numbers: Lift and drag coefficients. Computers & Fluids, 171, pp.53-64.

[50] Habib, R., Karimi, N., Yadollahi, B., Doranehgard, M.H. and Li, L.K.B., 2020. A pore-scale assessment of the dynamic response of forced convection in porous media to inlet flow modulations. International Journal of Heat and Mass Transfer, 153, p.119657.

[51] Nasiri, H., Jamalabadi, M.Y.A., Sadeghi, R., Safaei, M.R., Nguyen, T.K. and Shadloo, M.S., 2019. A smoothed particle hydrodynamics approach for numerical simulation of nano-fluid flows. Journal of Thermal Analysis and Calorimetry, 135(3), pp.1733-1741.

[52] Abdelmalek, Z., Alamian, R., Shadloo, M.S., Maleki, A. and Karimipour, A., 2020. Numerical study on the performance of a homogeneous charge compression ignition engine fueled with different blends of biodiesel. Journal of Thermal Analysis and Calorimetry, pp.1-11.